

4

2819

2820

Muon Phase-2 Upgrade

2821 In Chapter 2, the timeline of the LHC has been described and the upcoming High Luminosity LHC
2822 was introduced. LS3 has now started and the first HL-LHC related upgrade of CMS will take place.
2823 In order to understand the context in which the work of this thesis was performed as well as its
2824 motivations, it is necessary to give more insight into the reasons behind the increased instantaneous
2825 luminosity of LHC. In a first section of the chapter, these motivations will be discussed.

2826 The muon system of CMS will then be presented in greater details than what was done in Chapter
2827 ?? in order to have a better understanding of the need for upgrades of its different sub-systems in
2828 the perspective of HL-LHC. Most of the detectors will require new electronics to adapt to the new
2829 data flow and be integrated into a more robust trigger. Moreover, the redundancy of the muon system
2830 in the endcaps will need to be improved. This will be achieved by the addition of new detectors.

2831 Finally, some insight will be given on ecofriendly gas studies for the specific case of Resistive
2832 Plate Chambers. These studies don't fall into the scope of the HL-LHC upgrades but the necessity
2833 of operating the detectors with gas mixtures that are more respectful of the environment is real. The
2834 European union is starting to press the scientific community for solutions and the research institutes
2835 are investing time into finding replacements to the gases used while maintaining similar working
2836 performances.

2837 **4.1 Motivations for HL-LHC and the upgrade of CMS**

2838 As detailed in Section 2.2.2, the first data taking period, during which the LHC was only operated
2839 at a center-of-mass energy of 7 TeV, took place until the start of LS1. It has been sufficient to
2840 claim the discovery of a new $125 \text{ GeV}/c^2$ particle compatible with the Higgs boson by both CMS
2841 and ATLAS in July 2012 and hence achieve a major milestone in the history of science towards the
2842 understanding of the fundamental nature of the universe. Nevertheless, the LHC machine holds the
2843 potential to go further and help unravel the remaining mysteries the High-Energy Physics (HEP)
2844 community is facing.

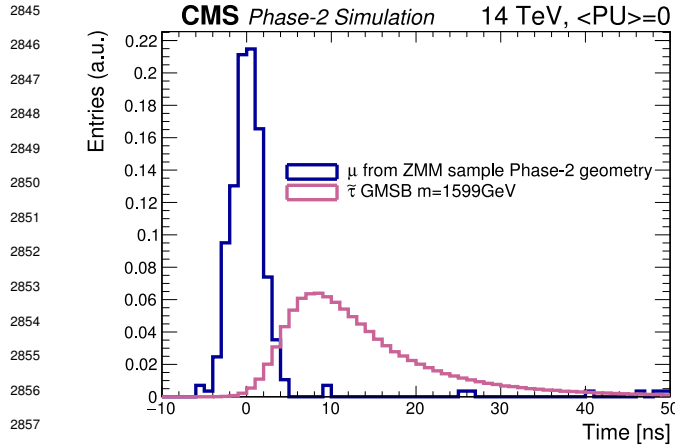


Figure 4.1: The measured transit time of an HSCP in CMS is compared to the transit time of a particle traveling at near the speed of light [177].

heavy gauge boson studies would also see their mass range limits pushed away by at least 1 TeV and could lead to a new breakthrough. Many of the Standard Model extensions discussed in Section 2.1.3 yield Heavy Stable Charged Particles (HSCPs), i.e. heavy long-lived particles. These particles would be produced at the LHC with a high momentum but a velocity significantly lower than the speed of light ($\beta < 0.9$) [238–242] and/or a charge that differs from the elementary charge ($|Q| = e$, $|Q| < e$ or $|Q| > e$) [241–246]. Depending on the model considered, HSCPs could be lepton-like heavy particles or on the contrary R-hadron, i.e. particles composed of a supersymmetric particle and at least one quark [241].

Over its full lifetime, the HL-LHC is expected to deliver an outstanding integrated luminosity of 3000 fb^{-1} , nearly an order of magnitude higher than what will be delivered by LHC until LS3 starts, as shown in Figure 2.20. In the case of Higgs studies, this will lead to measuring the couplings of the boson to a precision of 2 to 5%. Thanks to the estimated 15 millions of Higgs bosons created every year, a more precise measurement of potential deviations from the theoretical predictions is expected. The properties of the boson will hence be tested and compared to the SM Higgs neutral boson.

SUSY and

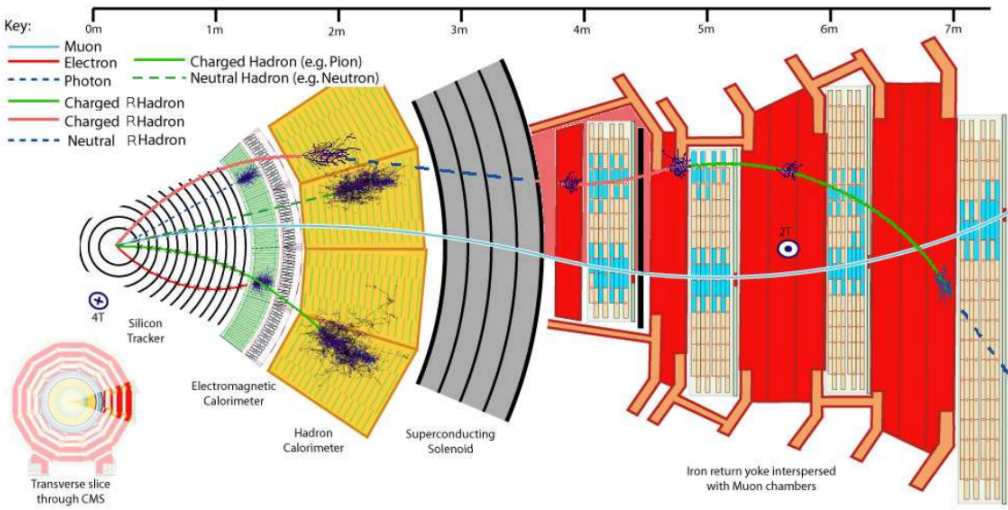


Figure 4.2: Slice of the CMS detector showing examples of passage of SM particles and R-hadrons. On the one hand, lepton-like HSCPs will appear to behave like slow and heavy muons. On the other hand, R-hadrons are likely to convert into other kind of charged or neutral R-hadrons due to interactions inside the detector volume.

2871 Due to lifetimes of the order of a few ns,
 2872 HSCPs would travel for long enough distances
 2873 to cross through entire typical collider detec-
 2874 tors while appearing almost stable. Because
 2875 of their low velocity, they can be reconstructed
 2876 and assigned to bunch crossings different to
 2877 the ones they effectively have been produced,
 2878 as shown in Figure 4.1, if reconstructed at
 2879 all. Indeed, the trigger algorithms in use at
 2880 CMS were not designed for such slow parti-
 2881 cles, and they assume most particles of inter-
 2882 est will have a velocity close to the speed of
 2883 light [242, 247].

2884 As HSCPs are long-lived particles, their
 2885 identification would be possible thanks to the
 2886 muon system. The main background will con-
 2887 sist of wrongly measured muons which should
 2888 have a lower transverse momentum, a near to
 2889 speed-of-light velocity and a low ionisation
 2890 energy loss. An example of passage of HSCPs
 2891 through a slice of the CMS detector is showed
 2892 in Figure 4.2. The tracks associated to the
 2893 HSCPs would then have to be reconstructed in
 2894 both the silicon detectors, for precise dE/dx
 2895 measurement, and the muon system detectors. In this case, the muon system will be used to perform
 2896 Time-of-flight (ToF) measurements to discriminate between near speed-of-light particles and slower
 2897 ones. The full reconstruction will then look for useful signatures such as the large transverse mo-
 2898 mentum of the candidates, or their large ionisation energy loss alongside the low velocity accurately
 2899 measured thanks to the muon system as depicted in Figure 4.3. The ToF measurement to identify
 2900 beyond the Standard Model particles will mostly rely on the time information provided by the Drift
 2901 Tubes, in the barrel region of the detector, and Cathode Strip Chambers, in the endcaps. From CMS
 2902 point of view, it will then become necessary to increase the acceptance and redundancy of the end-
 2903 caps toward higher pseudo-rapidity as the pseudo-rapidity region $1.6 < |\eta| < 2.5$ is only covered
 2904 by CSCs.

2905

2906 A natural consequence of the higher instantaneous luminosity will be the increase of collisions
 2907 per bunch crossing. It is estimated that the pile-up will rise from the approximate average of 40
 2908 collisions per bunch crossing in 2017 and 2018, presented in Figure 4.4, to 140 to 200 depending on
 2909 the scenario considered [248]. The trigger rate will then be affected in the same way putting a lot
 2910 of stress on the trigger algorithms. Upgrading the electronics of some of the detectors and working
 2911 on the data flow within the experiment would help going through HL-LHC with keeping similar
 2912 performance than during Phase-1. On the other hand, the impact of the increased background will
 2913 become problematic in many ways and will force for upgrades or many sub-systems of CMS. The
 2914 main effects will be a large increase of the irradiation of the detectors, mainly close to the beam
 2915 line. Both the detectors already installed and the new detectors that will extend the coverage of the

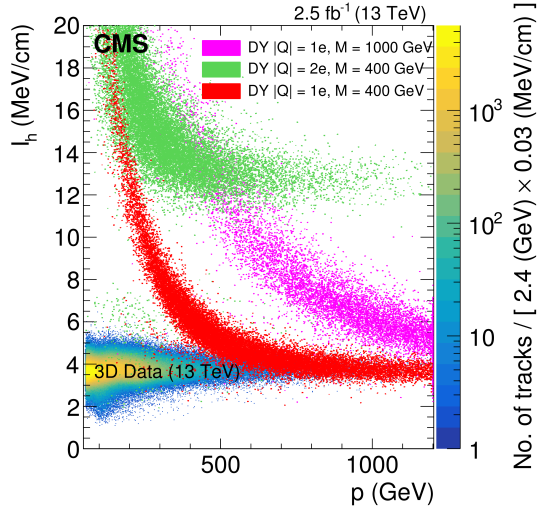


Figure 4.3: Distribution of the energy-loss dE/dx as described by Bethe-Bloch formula through the estimator I_h with increasing particle momentum for tracks in the 13 TeV data. The estimator depends on the charge deposition of the particles per unit length in the silicon detectors of CMS which is related to their energy loss as explained in a publication by the CMS Collaboration [241]. The simulated HSCPs are singly or multiply charged particles with masses of 400 and 1000 GeV.

muon system toward higher pseudo-rapidity need to be certified for the irradiation levels they will be subjected to until the end of HL-LHC. Simulations of the expected distribution of absorbed dose in the CMS detector under HL-LHC conditions show, in Figure 4.5, that detectors placed close to the beam line will have to withstand high irradiation, the radiation dose being of the order of a few tens of Gy.

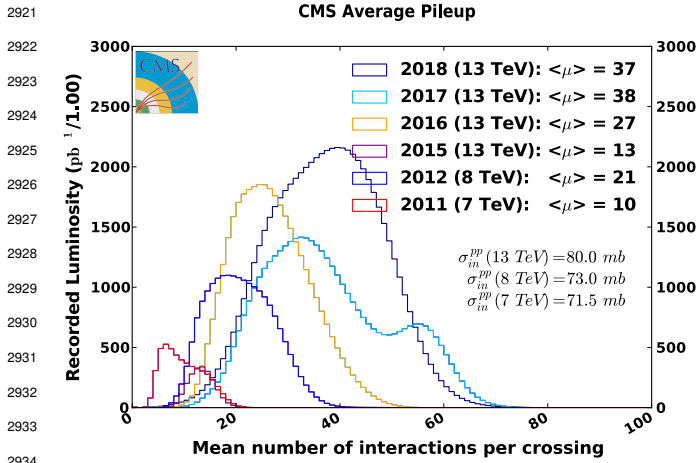


Figure 4.4: Distribution of the average number of interactions per crossing (pileup) for pp-collisions in 2011 (red), 2012 (blue), 2015 (purple), 2016 (orange), 2017 (light blue), and 2018 (navy blue). The overall mean values and the minimum bias cross sections are also shown [249].

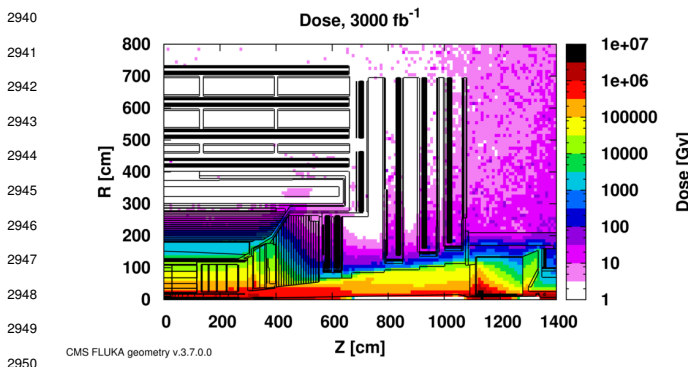


Figure 4.5: Absorbed dose in the CMS Cavern after an integrated luminosity of 3000 fb^{-1} . Using the interaction point as reference, R is the transverse distance from the beamline and Z is the distance along the beamline [177].

4.0 but the identification of muons and measurement of their energy with reasonable precision only using the tracker is nearly impossible. Thus, this increased tracker coverage range needs to be put in parallel with a matching muon detector and will open doors to multi-lepton final states in which leptons are likely to have a low transverse momentum and to be found near the beam line.

Finally, as the muon system is composed only of gaseous detectors, strong environmental concerns have risen over the last years as the European directives will restrict the use of fluorine based gas mixtures. Both the CSC and RPC subsystems, using CF_4 , $C_2H_2F_4$, or SF_6 , will need to adapt

Improving this situation will come with the increase of hit numbers recorded along the particle track to reduce the ambiguity on muon versus background detection. Moreover, the measurement of small production cross-section and/or decay branching ratio processes, such as the Higgs boson coupling to charge leptons, and in particular to muons, or the $B_s \rightarrow \mu^+ \mu^-$ decay, is of major interest. Such considerations give more weight to the upgrade of the forward regions to maximize the physics acceptance to the largest possible solid angle.

To ensure proper trigger performance within the present coverage, the muon system will be completed with new chambers, and the electronics of the present system will need to be upgraded. A first step into this direction will be taken by installing new gaseous detectors in each endcap layer and extend the coverage up to $|\eta| = 2.8$. Nevertheless, the region beyond $|\eta| > 2.8$ and extending to $|\eta| = 5.0$ only is covered by the forward HCAL detectors and lack redundant muon detector coverage. Extensions of the tracker in the context of HL-LHC will increase its coverage up to $|\eta| =$

their working gas in order to strongly reduce the greenhouse potential of the mixtures released into the atmosphere due to gas leaks.

4.2 Necessity for improved electronics

Drift Tubes and Cathode Strip Chambers are important components used to identify and measure muons, especially thanks to their spatial resolution of the order of 100 μm . Nevertheless, the luminosity and irradiation during HL-LHC will cause serious event loss and ageing on the electronics of these subsystems that will comprise the triggering and data transferring needs of CMS. Thus, electronics upgrade is foreseen to address these expected problems. While only the RPCs' electronic system is able to operate under Phase-2 requirements [250], DTs and CSCs will need to improve their trigger acceptance rate and latency to ensure that the Level-1 trigger threshold can stay at the same level [251]. The Level-1 trigger consists of custom hardware processors receiving data from the calorimeters and the muon system. In return, they generate a trigger signal within 3 μs , with a maximum rate of 100 kHz. In the perspective of HL-LHC, each subsystem needs to achieve a minimum rate of 500 kHz with a latency not greater than 12.5 μs . DTs and CSCs will also need to improve their Data Acquisition (DAQ) transfer rate to reach a minimum near 1 Tbit/s. The foreseen upgrades are expected to exceed the requirements.

The first version of Minicrate electronics (MiC1) used by DTs don't allow for high enough trigger rate. In addition to this problem, it was shown that these electronics contain components that are not radiation hard enough to sustain HL-LHC conditions and hence, a too large number of channels may fail due to radiations as showed in Figure 4.6. The MiC1 will be replaced on each detector by an improved version referred to as MiC2 while Front-End Electronics (FEE) and High Voltage (HV) modules will not need any replacement. On the other hand, CSCs showed that their electronics would be

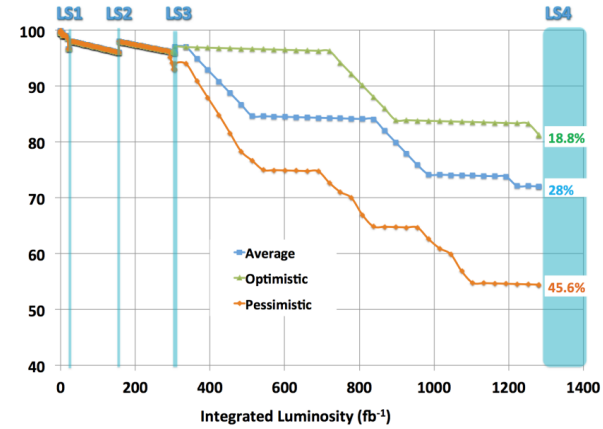


Figure 4.6: Extrapolated fraction of failing channels of the present DT MiC1 electronics as a function of the integrated luminosity for different scenarios until LS4 [177].

The first version of Minicrate electronics (MiC1) used by DTs don't allow for high enough trigger rate. In addition to this problem, it was shown that these electronics contain components that are not radiation hard enough to sustain HL-LHC conditions and hence, a too large number of channels may fail due to radiations as showed in Figure 4.6. The MiC1 will be replaced on each detector by an improved version referred to as MiC2 while Front-End Electronics (FEE) and High Voltage (HV) modules will not need any replacement. On the other hand, CSCs showed that their electronics would be

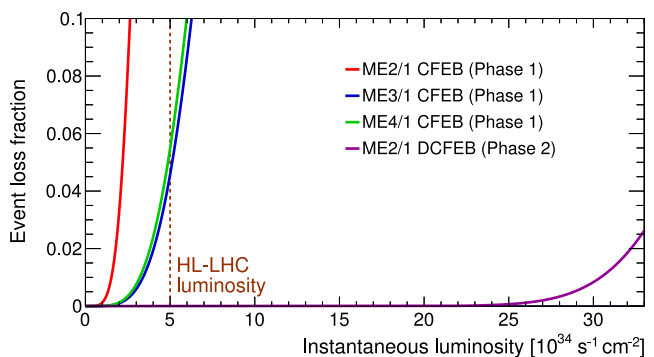


Figure 4.7: The event loss fractions as a function of the instantaneous luminosity is compared for CFEBs (Phase-1) and DCFEBs (Phase-2) at different CSC locations. HL-LHC luminosity is marked with the dashed brown line [177].

able to live through the 10 years of Phase-2, but the limited buffer depth might cause memory overflows and read-out inefficiencies with a fraction of event loss ranging from 5 to more than 10% at an instantaneous luminosity similar to which of HL-LHC depending on the expected background. The replacement of CSCs' CFEBs by digital ones, DCFEBs, with a deeper buffer would permit to make event loss negligible and satisfy HL-LHC requirements as can be seen in Figure 4.7. All these new DT and CSC electronics will be connected to the trigger electronics via optical links to ensure a faster communication [177].

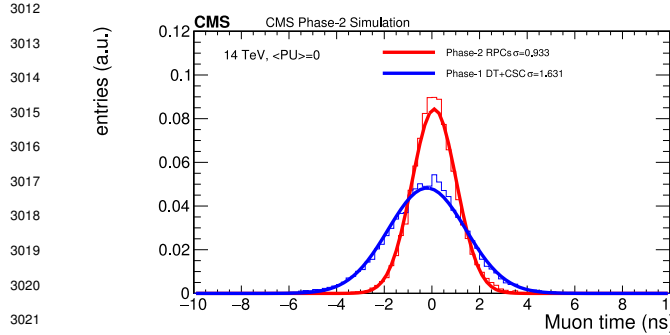


Figure 4.8: Comparison of the simulated time residuals in between reconstructed and true muon times without (blue) and with (red) the upgraded RPC link system [177].

ponents may become the source of failing channels throughout Phase-2. Moreover, these link boards were originally designed only to match RPC digitized signals with the corresponding bunch crossing. Due to this feature, the time resolution of the full RPC chain is hence limited to 25 ns and does not make use of the full time resolution of the detectors. The time resolution foreseen after the upgrade can be seen through Figure 4.8 and is of the order of 1 ns.

The upgrade on the side of Resistive Plate Chambers will not be done at the level of the electronics but rather that of the Link System located in the service cavern of CMS. RPC Link System connects the front-end electronics data of RPCs into CMS trigger processors. The main motivation for such an upgrade is that the electronic board composing the link system are built using obsolete and/or weak components that can easily suffer from the electromagnetic noise. These com-

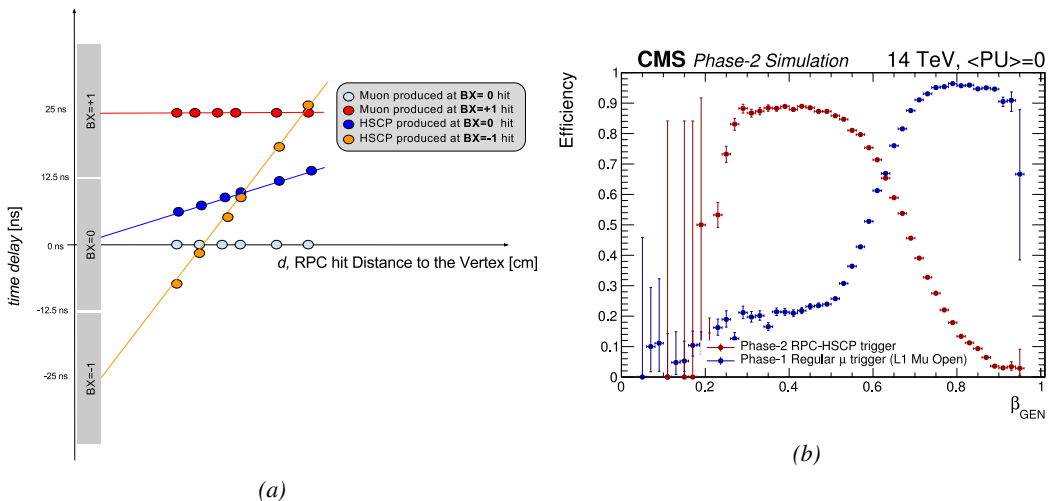


Figure 4.9: (a): Time delay with respect to a particle traveling at the speed of light measured at consecutive RPC stations for particles originating at different bunch crossings and traveling at different velocities [177]. (b): In blue is showed the standard Level-1 muon trigger efficiency as a function of β and in red is showed the RPC-HSCP trigger efficiency after upgrade of the RPC Link System [177].

The exploitation of the full time resolution would make the synchronization of the RPC system easier and allow to have a finer offline out-of-time background removal within the 25 ns between consecutive bunch crossings. Moreover, this would greatly improve the trigger and reconstruction on HSCPs. Using the TOF information in between consecutive RPC stations, the minimal particle velocity than could be probed will drop from approximately 0.6 to 0.25 times the speed of light as showed in Figure 4.9. Upgrading RPC link system will require the installation of 1376 new link boards and 216 control boards. The new boards will make use of the recent progress made with fast FPGAs and will be a great improvement to the ASICs formerly used as they will be able to process signals from several detectors in parallel.

4.3 New detectors and increased acceptance

In the present muon system, the redundancy is assured by RPCs used for their robust bunch crossing assignments. The extension of the muon system towards higher pseudo-rapidity in an effort to complete the redundancy and to contribute to the precision of muon momentum measurements will require muon chambers with a spatial resolution less or comparable to the multiple scattering muons are subjected to while traveling through the detector volume [192].

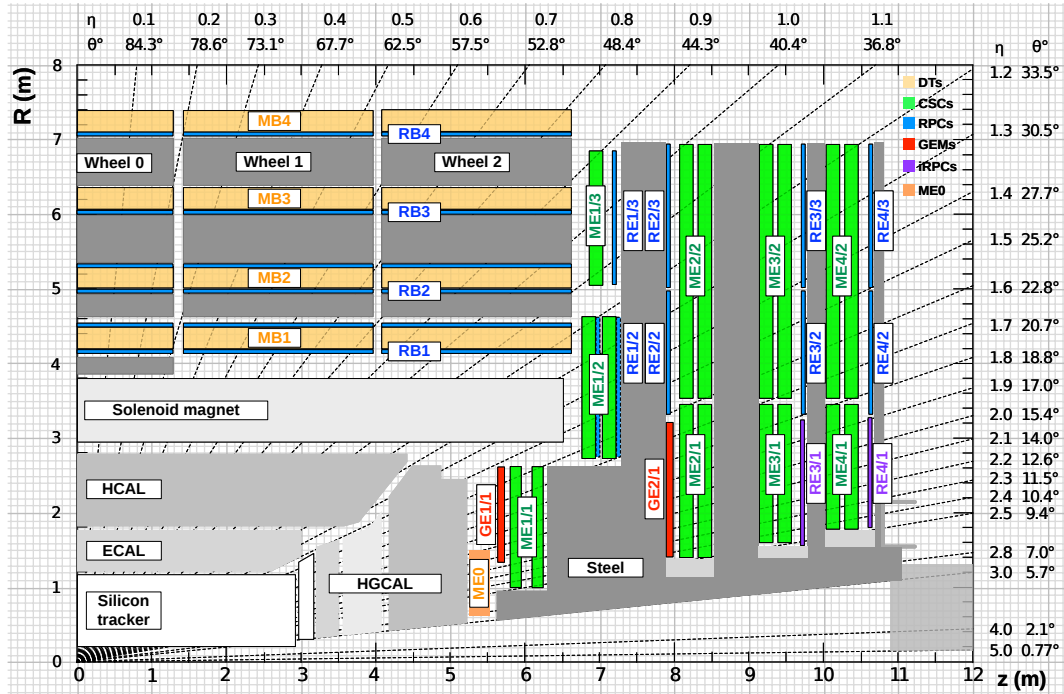


Figure 4.10: A quadrant of the muon system, showing DTs (yellow), RPCs (blue), and CSCs (green). The locations of new forward muon detectors for Phase-2 are contained within the dashed box and indicated in red for GEM stations (ME0, GE1/1, and GE2/1) and dark blue for improved RPC (iRPC) stations (RE3/1 and RE4/1).

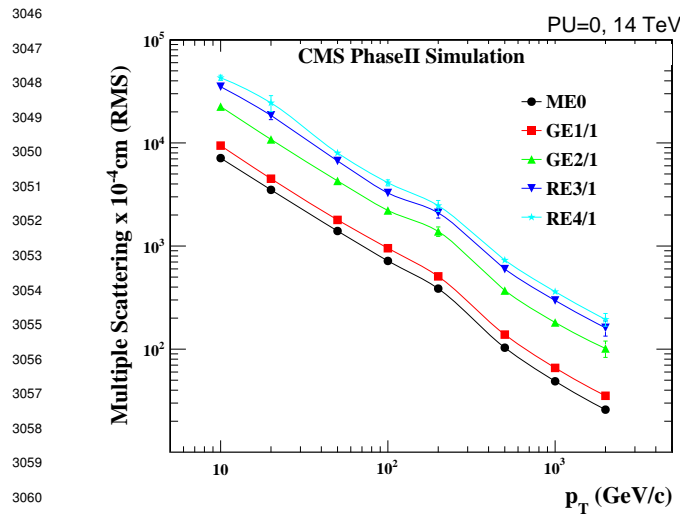
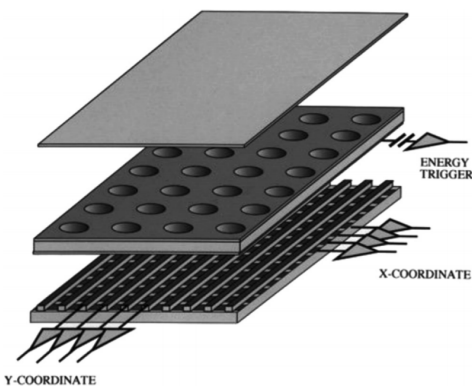


Figure 4.11: RMS of the multiple scattering displacement as a function of muon p_T for the proposed forward muon stations. All of the electromagnetic processes such as bremsstrahlung and magnetic field effect are included in the simulation.

showed by the simulation in Figure 4.11. Indeed, most of the plausible physics will be covered only considering muons with $p_T < 100$ GeV.

3068 4.3.1 Gas electron multipliers



3081 *Figure 4.12: Schematics of a GEM. On top is the cath-*
 3082 *ode and on the bottom, the anode on which a 2D read-*
 3083 *out is installed. Finally, the GEM foil separates the gas*
 3084 *volume into the drift region, in between the cathode and*
 3085 *the foil, and the induction region, in between the foil and*
 3086 *the anode. A negative voltage is applied on the cathode.*
The anode is connected to the ground.

3088 volume is confined between two planar electrodes, the anode serving as read-out panel. The gas vol-

Figure 4.10 shows a similar quadrant of CMS than the one presented in Figure 2.27 with the addition of Gas Electron Multiplier (GEM) (ME0, GE1/1 and GE2/1) and improved RPC (iRPC) (RE3/1 and RE4/1) in the pseudo-rapidity region $1.6 < |\eta| < 2.4$. The completion of the redundancy was already scheduled in the original CMS Technical Proposal [252] but never addressed. The coming Phase-2I is then the occasion to equip the region with the newest GEM and RPC technology. In order to match CMS requirements, a spatial resolution of $\mathcal{O}(\text{few mm})$ will be necessary for the proposed new RPC stations while the GEMs will need a resolution better than 1 mm, as

In the region closer to the interaction point where the spatial resolution is requested for the new detectors to be better than 1 mm (at least for ME0 and GE1/1 according to Figure 4.11) and where the background rate will be the highest for muon detectors, the choice has been made to use triple GEMs, micro pattern gaseous detectors, instead of the originally planned RPCs. The GE1/1 project has been the first to be approved and demonstrators have been installed in CMS already during LS1. The rest of the detectors will be installed during LS2 while the GE2/1 and ME0 projects are still under development. ME0, GE1/1 and GE2/1 will be installed respectively close to the HCAL endcap, on the first and on the second muon endcap disks as can be seen from Figure 4.10. Gas Electron Multipliers are gaseous detectors [253] whose gas

3089 ume is divided in two or more regions by a single or multiple *GEM foils* as showed in Figure 4.12.

3090 These foils are very thin, of the order of a
 3091 few tens of μm , and are pierced with holes as
 3092 can be seen in Figure 4.13. Both surfaces of
 3093 the GEM foils are clad with copper in order
 3094 to apply a strong electric field in between each
 3095 side that will generate very strong potentials
 3096 in the holes. The gas region contained in be-
 3097 tween the cathode and the GEM foil is called
 3098 the drift region as the electric field is not strong
 3099 enough to cause avalanches and thus start an
 3100 amplification. The primary electrons drift to-
 3101 ward the foil and are accelerated and amplified
 3102 by the very high potential within the holes,
 3103 as showed in Figure 4.13. Then the electrons
 3104 reach the second drift region where they will
 3105 induce a signal on the read-out located on the
 3106 anode. By restraining the amplification pro-
 3107 cess at the level of the holes, the electrons
 3108 can stay confined in a very little space and
 3109 thus induce a very localized current, provid-
 3110 ing the GEMs with a very good spatial res-
 3111 olution. The process can be repeated several
 3112 times in a row, in order to achieve a stronger
 3113 amplification. The GEMs that will be used in
 3114 CMS are triple-GEM detectors operated with
 3115 a 70/30 gas mixture of Ar/CO_2 . They con-
 3116 tain three GEM foils and hence three electron
 3117 amplifications, as can be seen in Figure 4.14.

3118 The GEM foils used in CMS are
 3119 50 μm foils clad with 5 μm of copper
 3120 on each side. The foils are pierced
 3121 with double-canonical holes which
 3122 inner and outer diameters are re-
 3123 spectively 50 and 70 μm which are
 3124 placed 140 μm from each other in
 3125 a hexagonal pattern, as showed in
 3126 Figure 4.13. These detectors have a
 3127 time resolution better than 10 ns and
 3128 reach very good spatial resolutions
 3129 of less than 200 μrad as indeed the
 3130 position of the hits is not measured
 3131 along the strips but following the az-
 3132 imuthal angle granularity of the ra-
 3133 dially organized trapezoidal strips.

3134 The GEM Upgrade project started with GE1/1 [254]. GE1/1 detectors will already be installed

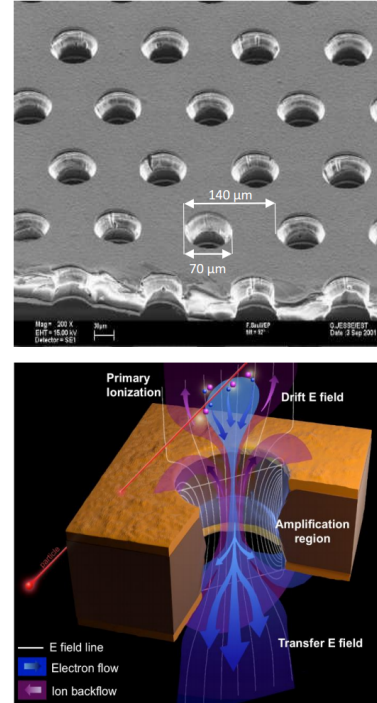


Figure 4.13: Top: Picture of a CMS GEM foil provided by a scanning electron microscope. Bottom: Representation of the electric field in a GEM hole and of the amplification electrons and ions undergo due to the very intense electric field.

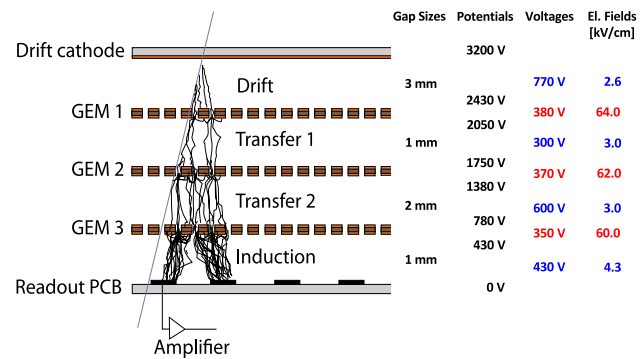


Figure 4.14: The gas volume of CMS triple-GEMs is divided into four areas. Primary electrons are created in the Drift area and amplified by three GEM-foils while drifting through Transfer areas. Reaching the Induction area, the avalanche induces current in the read-out. The typical dimensions and potentials are provided.

3135 during LS2. GE2/1 and ME0, on the other hand, will profit of the R&D knowledge and skills
 3136 developed for GE1/1 while the requirements for each subsystem are different as they are not placed
 3137 at the same distance from the interaction point. In this very forward region, a different position with
 3138 respect to the center of the detector can dramatically change the conditions in which the detectors
 3139 will have to be operated. In terms of rate capability, GE2/1, which is the furthest, is required to
 3140 withstand 2.1 kHz/cm^2 while GE1/1 needs to be better than 10 kHz/cm^2 and ME0, better than
 3141 150 kHz/cm^2 . In terms of ageing with respect to charge deposition, ME0 needs to be certified to
 3142 840 mC/cm^2 , GE1/1 to 200 mC/cm^2 and GE2/1 only to 9 mC/cm^2 . All 3 detectors need to have a
 3143 time resolution better than 10 ns and an angular resolution better than $500 \mu\text{rad}$.

3144 On each GE1/1 ring, 36 super chambers, consisting of two single GEM layers and spanning 10° ,
 3145 will be installed covering the pseudo-rapidity region $1.6 < |\eta| < 2.2$ together with ME1/1 CSCs.
 3146 The reach of the muon system will be improved thanks to the GE2/1 that will overlap with the GE1/1
 3147 and cover a region from $|\eta| > 1.6$ to $|\eta| < 2.4$ and complete the redundancy of ME2/1. The super
 3148 chambers, built with two triple-GEM layers each consisting of four single GEM modules due to
 3149 the rather large surface of the GE2/1 chambers, that will be installed on the first ring of the second
 3150 endcap will span 20° each. Hence, a total of 72 chambers will be assembled to equip the muon
 3151 system. Finally, the ME0 installed near the HCAL endcap will cover the region $2.0 < |\eta| < 2.8$.
 3152 This subsystem will consist in super modules of six layers of triple-GEM detectors covering an
 3153 azimuthal angle of 20° leading to the construction of 216 single detectors.

3154 Adding the GEMs into the forward region of the muon system will allow to strongly enhance
 3155 the Level-1 Trigger performance as shown in Figure 4.15. In the region $1.6 < |\eta| < 2.4$, the trigger
 3156 efficiency of the current system would lie between 80 and 90% under HL-LHC conditions. The
 3157 installation of GEMs would bring the efficiency to a consistent 92 to 94% on the entire region. At
 3158 the same time, the trigger rate is expected to fluctuate from 3 to 10 kHz with the current system
 3159 alone. The addition of detectors to complete the redundancy would allow keeping the rate mostly
 3160 under 2 kHz. Moreover, benefiting from the good spatial and angular resolution of the GEMs, the
 3161 precision into the muon measurement will also be improved by an order of magnitude thanks to the
 3162 addition of GEMs as can be seen from the simulation presented in Figure 4.16.

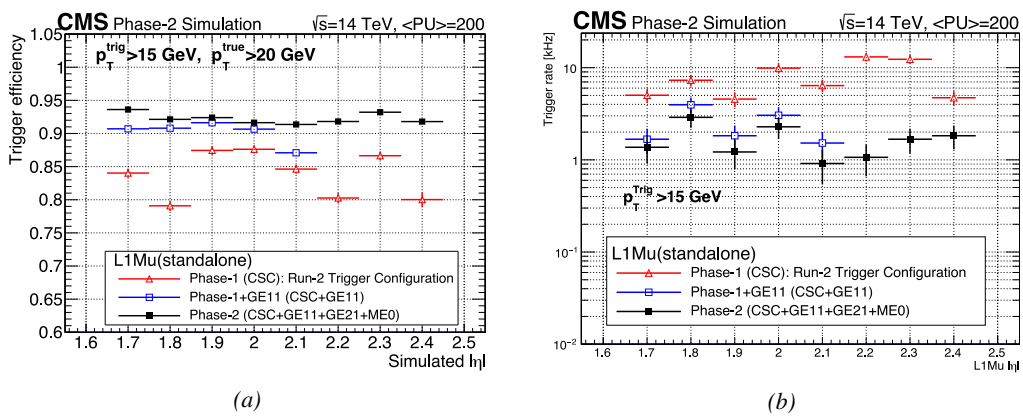


Figure 4.15: Simulated (a) efficiency and (b) rate of the standalone Level-1 muon trigger using tracks reconstructed in CSCs and all GEM stations compared with Phase-I values in the case where only CSCs are used or CSCs+GE1/1. The zones of inefficiency of the CSC subsystem are compensated by the addition of GEMs during Phase-2 and the trigger rates is kept from increasing due to the high luminosity [177].

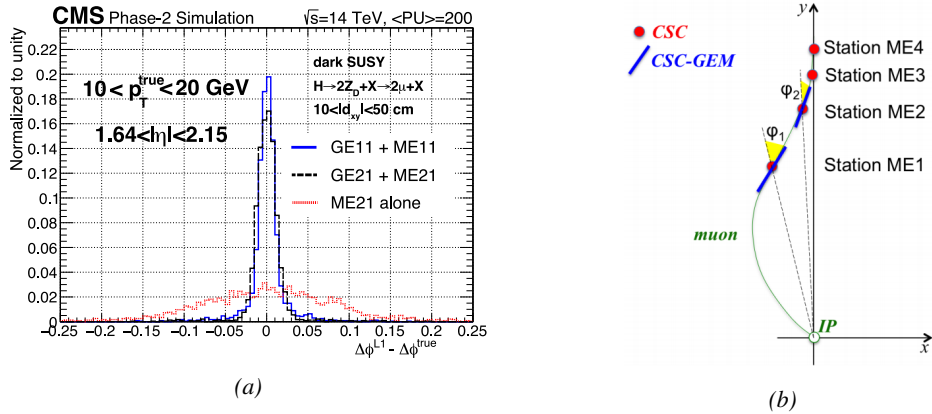


Figure 4.16: (a): Simulated resolution of the muon direction measurement $\Delta\phi$ with Phase-2 conditions. In the second endcap station, the resolution is compared in the case of CSCs (ME2/1) alone and CSCs+GEMs (GE2/1+ME2/1) while a similar resolution measurement is given in the case of the first station (GE1/1+ME1/1) [177]. (b): The addition of GEM detectors on stations 1 and 2 (ME0 is considered to contribute to station 1) as redundant system to CSCs allows improving the muon momentum improvement through a more accurate measurement of the local bending angles ϕ_1 and ϕ_2 [177].

3163 4.3.2 Improved forward resistive plate chambers

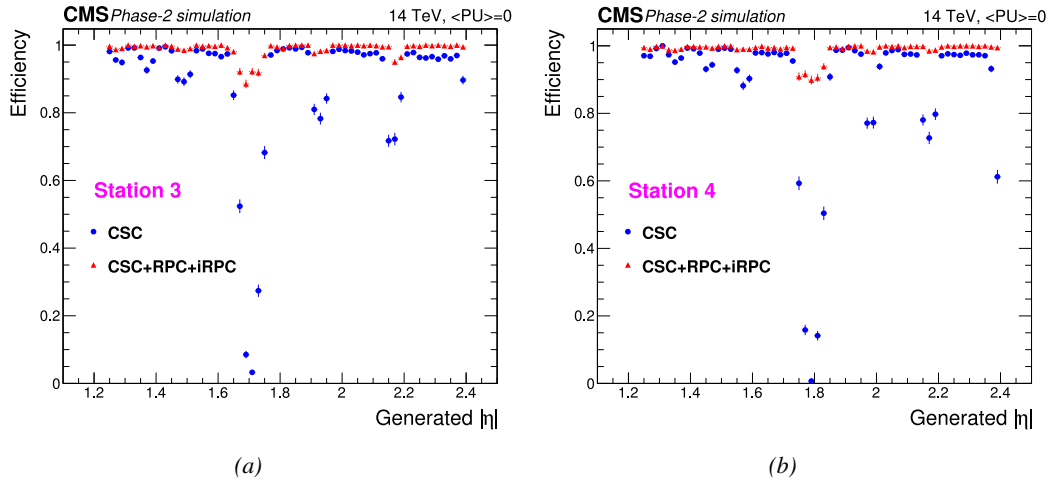


Figure 4.17: Simulation of the impact of RPC hit inclusion onto the local trigger primitive efficiency in station 3 (a) and station 4 (b) [177]. The contribution of iRPC starts above $|\eta| = 1.8$.

3164 Figure 4.10 shows that the iRPCs that will equip the third and fourth endcap disks in position RE3/1
 3165 and RE4/1 will finally be the partners of the CSCs in position ME3/1 and ME4/1. They will complete
 3166 Phase-1 plans by bringing the needed upgrades in the perspective of Phase-2 as the older chambers
 3167 are not suitable to equip the forward region of CMS due to HL-LHC rates and charge deposition.
 3168 By completing the redundancy, more hits along the muon track will be available and the lever arm
 3169 will be improved. The benefits from extending the redundancy of the muon system with iRPCs to

3170 the forward most region is shown in Figure 4.17 in which the trigger efficiency is presented with and
 3171 it is possible to see that the efficiency of the CMS muon trigger with the complete
 3172 redundancy is consistently improved to a level above 95% in the region $|\eta| > 1.8$ as the iRPCs help
 3173 filling the holes in the CSC system.

3174 The detectors that will be installed in the coming years will have similarities with the already
 3175 existing RPC system. 18 of the new chambers, each spanning 20° in φ around the beam axis with
 3176 96 radially oriented trapezoidal read-out strips, will cover each muon endcap disk leading to the
 3177 production of 72 iRPCs. The main difference with the old RPC detectors will be found at the level
 3178 of the read-out panels. Indeed, the new chambers will not feature read-out strips segmented in η
 3179 but rather will favor a read-out on both strip ends to determine the position of the hits along the
 3180 chamber. By using fast front-end electronics a radial spatial resolution of the order of 2 cm could
 3181 be achieved to contribute to the better reconstruction of muons in the forward region where the
 3182 bending due to the magnetic field is low. This technical choice is motivated by the fact that, in
 3183 the case a η segmentation were to be used, at least five pseudo-rapidity partitions would have been
 3184 necessary to reach the minimal radial spatial resolution (≈ 20 cm). Having only one strip along the
 3185 chamber read-out from both ends reduces by 60% the total number of channels and the necessary
 3186 cabling, and allows for a better spatial resolution. The strip pitch will range from 6.0 mm (5.9 mm)
 3187 on the high pseudo-rapidity end to 12.3 mm (10.9 mm) on the low one on position RE3/1 (RE4/1).
 3188 The spatial resolution in the direction perpendicular to the strips should reach approximately 3 mm,
 3189 better than the minimal needed resolution (Figure 4.11). Finally, the overall time resolution of the
 3190 new installation will be equally 1 ns, as for the present due to the same link system being used even
 3191 though the detector itself can achieve a time resolution of less than 100 ps, necessary for a spatial
 3192 reconstruction of the hits with a resolution of 2 cm or less along the strip length.

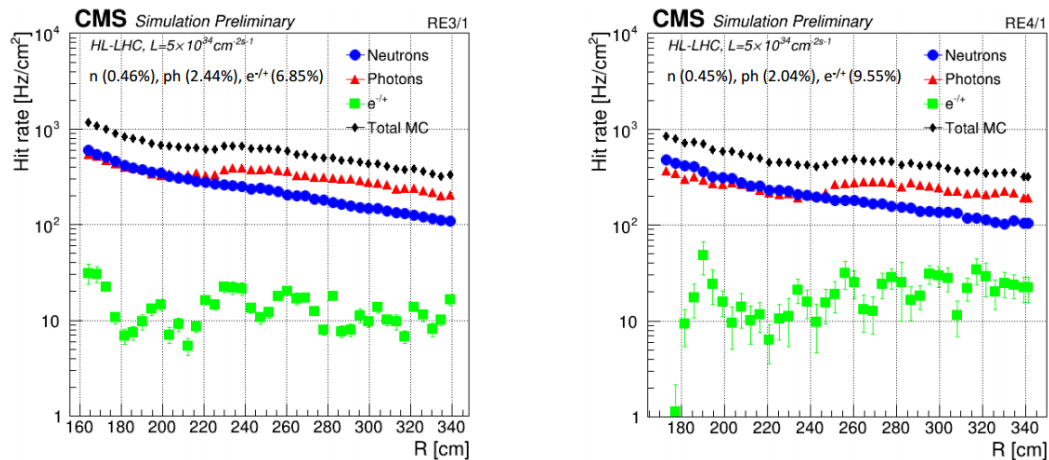


Figure 4.18: Expected hit rate due to neutrons, photons, electrons and positrons at HL-HLC instantaneous luminosity of $5 \times 10^{34} \text{ cm}^{-2}\text{s}^{-1}$ in RE3/1 and RE4/1 chambers [255, 256]. The sensitivities of iRPCs used in the simulation for each particle are reported and differ from one endcap disk to another as the energies of the considered particles varies with the increasing distance from the interaction point.

3193 Having only a single strip instead of pseudo-rapidity segmentation will increase the probability
 3194 of double hits in the same channel. The probability was estimated to be low enough as it shouldn't
 3195 exceed 0.7%. This estimation was made assuming an average hit rate per unit area of 600 Hz/cm²

in the iRPCs (see Figure 4.18), a cluster size (average number of strips fired per muon) of 2, a strip active area of $158.4 \times 0.87 \text{ cm}^2$ and a safety factor 3. The corresponding rate per strip is estimated to be 380 kHz leading to an average time interval in between two consecutive hits of 2600 ns. This is compared to the minimal time interval of 16 ns necessary to avoid ambiguities. Indeed, a maximum of 10 ns is spent by the signal traveling through the strip to reach the electronics to which can be added 1 ns of dead time and 2 Time-to-Digital Converter (TDC) clock cycles of 2.5 ns to convert the signal arrival time into a digital value in the FEEs. The probability of having ambiguous double hits in a strip is then the ratio between the minimal time interval in between two consecutive hits and the average time interval estimated from the rate the detectors would be subjected to.

The instantaneous luminosity at HL-LHC being very high, the rates at the position of the new chambers needed to be simulated in order to understand the necessary requirements for these detectors. The simulated results for different background components (neutrons, photons, electrons and positrons) are shown in Figure 4.18 assuming known sensitivities to these particles. It is shown that on average over the iRPC areas the rates would be of the order of 600 Hz/cm^2 (600 Hz/cm^2 seen in RE3/1 and 480 Hz/cm^2 in RE4/1) [255, 256]. Thus, taking into account a safety factor of about 3, it was decided that improved RPCs should at least be certified for rates reaching 2 Hz/cm^2 which will be achieved thanks to several improvements on the design and on the electronics. The detectors design will be based on the existing RPCs as they will also feature double RPC gaps. Similarly to the existing RPC system, the electrode material will be HPL although the thickness of the electrodes and of the gas gap will be reduced to 1.4 mm as a thinner gas gap leads to a decrease of deposited charge per avalanche as showed in Figure 4.19. The charge deposition in the case of 1.4 mm thick electrodes is reduced by a factor greater than 5 when compared to 2 mm electrodes at a similar electric field. The smaller the gas gap, the more the detector becomes sensitive to gap non-uniformities across the electrode planes, making a gap of 1.4 mm a good compromise in between these two competing factors.

A lower charge deposition inside of the detector volume means a slower ageing and a longer lifetime for detectors subjected to high irradiation. But, in order to take advantage of the lower detector gain, more sensitive electronics are required such that part of the gain that was formerly achieved in the gas volume can be moved to the electronics. Achieving this with the technology developed more than ten years ago for the present system is not possible as the signal over noise ratio of such electronics doesn't allow to detect charges as low as 10 fC. Moreover, the new front-end electronics will need to be radiation hard to survive more than ten years of HL-LHC conditions. The new technology that has been chosen is based on the PETIROC ASIC manufactured by OMEGA and is a 64-channel ASIC called CMS RPCROC[177, 257, 258]. The properties of these electronics will be discussed in Chapter 6.

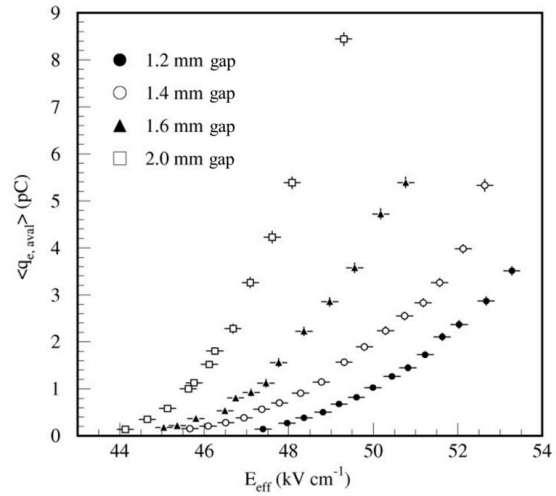
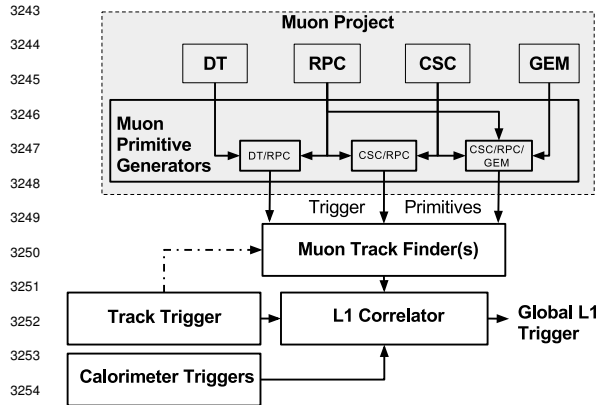


Figure 4.19: Measured average charge per avalanche as a function of the effective electric field for different gas gap thickness in double-gap RPCs using HPL electrodes [177].

3242 4.4 Impact on Level-1 Trigger and physics performance



3243
3244
3245
3246
3247
3248
3249
3250
3251
3252
3253
3254
3255
3256
3257
3258
3259
3260
3261
3262
3263
3264
3265
3266
3267
3268
3269
3270
3271
3272
3273
3274
3275
3276
3277
3278
3279
3280
3281
3282
3283
3284
3285
3286
Figure 4.20: Level-1 Trigger data flow during Phase-2 operations [177].

The upgrades of the different subsystems will have a subsequent impact on the Level-1 Trigger. Indeed, although its main scheme will not be affected, the efficiency of the trigger in identifying muons and provide the DAQ with good and fast trigger that can cope with HL-LHC instantaneous luminosity is a major improvement. In addition to the upgrade of the muon system in terms of trigger accept rate and latency, the Level-1 Trigger will get extra information by including the Tracker Trigger into its Muon Track Finder logic and combine the L1 Muon Trigger with Tracker and Calorimeter Triggers to generate a Global L1 Trigger, as shown in Figure 4.20. Using the

track candidates of both the muon system and the tracker in spatial coincidence will allow for a much better momentum resolution thanks to better identified muons and, hence, better measured transverse impulsion as described in reference [177].

In terms of muon trigger, three regions are considered due to their different track finding logic: the Barrel Muon Track Finder (BMTF), the Endcap Muon Track Finder (EMTF) for both the barrel and endcap regions, and finally the Overlap Muon Track Finder (OMTF) which concerns the pseudo-rapidity region in which there is a common coverage by both the barrel and endcap muon systems. This region can be seen in Figure 4.10 for $0.9 < |\eta| < 1.2$ and requires a specific more complex logic to provide an efficient reconstruction of muons due to the different orientation of the detectors and of the more complex magnetic field of this region. The development of a track finder specific to the overlap region was achieved during the Phase-1 upgrade of the L1-Trigger [259].

The upgraded RPC link system, allowing to take profit of the full 1 ns resolution of the detectors, will help reducing the neutron induced background, slightly improve the bunch crossing assignment, and help increasing the trigger efficiency in every sector. The upgrade of DT electronics is also to take into account as the trigger primitive generator will be renewed through the use of TDCs that will send the digitized signals directly to common DT/RPC back-end electronics instead of having an on-detector trigger logic as it will be the case until the end of Phase-1. The combination of RPC hits together with DT primitives will bring extra improvement in the bunch crossing assignment in the barrel and overlap regions and improve the efficiency of the trigger between the wheels were the quality of DT primitives is the poorest.

The current EMTF already uses more sophisticated algorithms by combining together RPC hits and CSC primitives. The GEMs, in stations 1 and 2, and the iRPCs, in stations 3 and 4, will be added into the EMTF algorithm. Both these contributions will help increase the efficiency of the L1 trigger in the endcap region in one hand, as showed by Figure 4.21, and help lowering the L1 trigger rate in the other hand, especially in the most forward region. Similarly to the RPC/CSC algorithms, data from both CSCs and GEMs are combined into the Optical TMBs (OTMBs) to build on each station, GEM/CSC primitives matching space and time information from both subsystems. The efficiency improvement and rate reduction close to the beam line will be naturally enhanced by the addition of more hits along the muon tracks, as can be seen from Figure 4.22 that focuses especially in the

most challenging pseudo-rapidity region. Indeed, the contribution from the GEMs to the lever arm of each track thanks to their high angular resolution will be a great asset in achieving such results, as can be seen in Figure 4.23. The rate will be partly reduced in the forward region thanks to the better spatial resolution of iRPCs, with respect to the current RPC system. The ambiguity brought by multiple local charged tracks in CSCs will be reduced, as explained through Figure 4.24. Indeed, as the rates will increase, the probability to record more than a single local charged track will greatly increase. This is due to the fact that the trigger algorithm uses information from three consecutive bunch crossings to find muon tracks. It is estimated that with iRPCs operated at 95% efficiency the resolution of ambiguous events would be of the order of 99.7%.

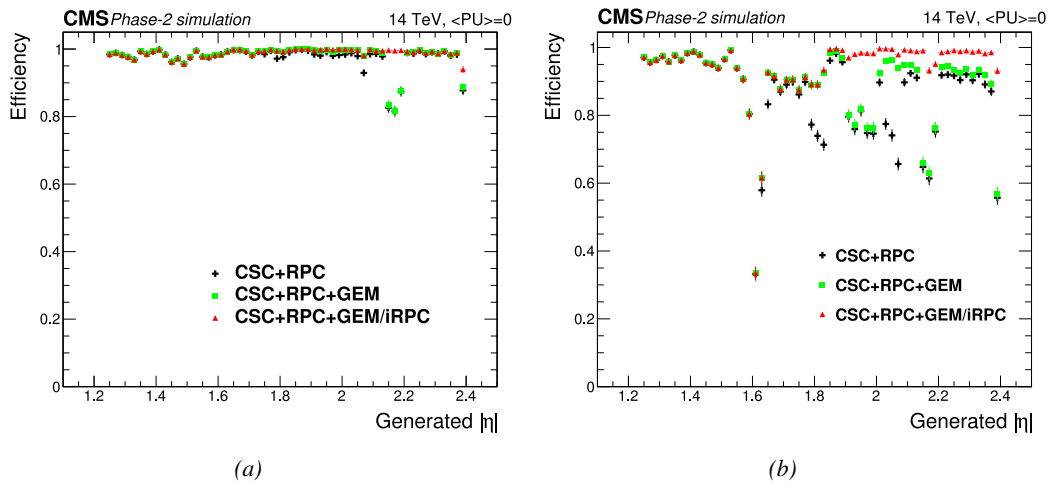


Figure 4.21: Efficiency of the L1 trigger in the endcap region after Phase-2 upgrade in the case CSC/GEM/RPC hits are requested in at least two stations out of four (a) and in all four stations (b) [177].

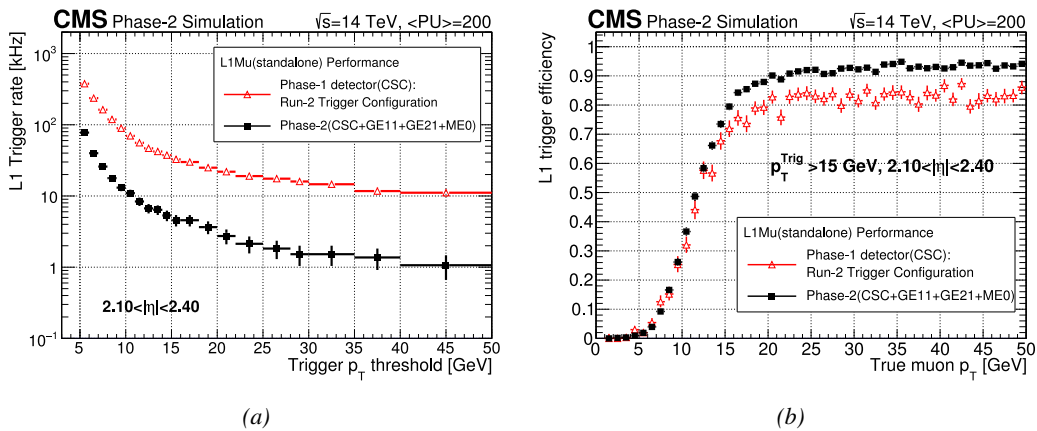


Figure 4.22: Comparison of L1 trigger performances for prompt muons with and without the addition of GEMs in the region $2.1 < |\eta| < 2.4$ at Phase-2 conditions [177]. GEMs would allow a reduction of the trigger accept rate by an order of magnitude (a) while increasing the trigger efficiency (b).

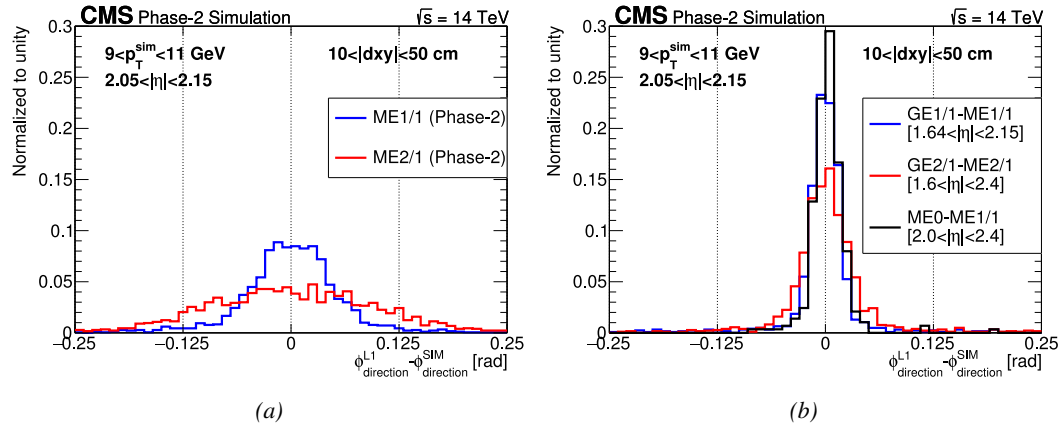


Figure 4.23: The angular resolution on reconstructed muon tracks in the GEM overlap region $2.0 < |\eta| < 2.15$ is compared for Phase-2 conditions in the case CSC are alone (a) and in the case the GEMs' data, including ME0, is combined to which of CSCs (b) [177].

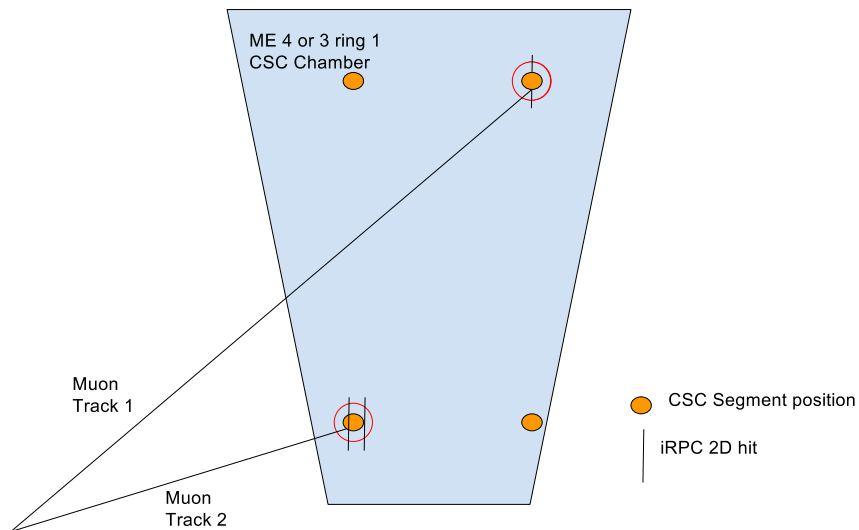


Figure 4.24: Resolution of the LCT ambiguous events thanks to the combination of CSC and iRPC readout data. Using CSCs only, two pairs of hits are possible [177].

4.5 Ecofriendly gas studies

In the last steps of R&D, the gas mixture of CMS RPCs was foreseen to be a 96.2/3.5/0.3 composition of $C_2H_2F_4/i-C_4H_{10}/SF_6$ [205] but finally it was slightly changed into a 95.2/4.5/0.3 mixture of the same gases [260]. A summary of the operation performance of the RPCs since the start of LHC and of CMS data taking is given in Figure 4.25 [261]. The performance of the detectors is regularly monitored and the operating voltages updated in order to obtain a very stable performance through time. Nevertheless, the detectors will face new challenges during Phase-II during which they will be exposed to more extreme radiation conditions. Description of the longevity tests with extreme

3304 irradiation and the conclusions regarding the operation of the present RPC system will be given in
 3305 Chapter 5.

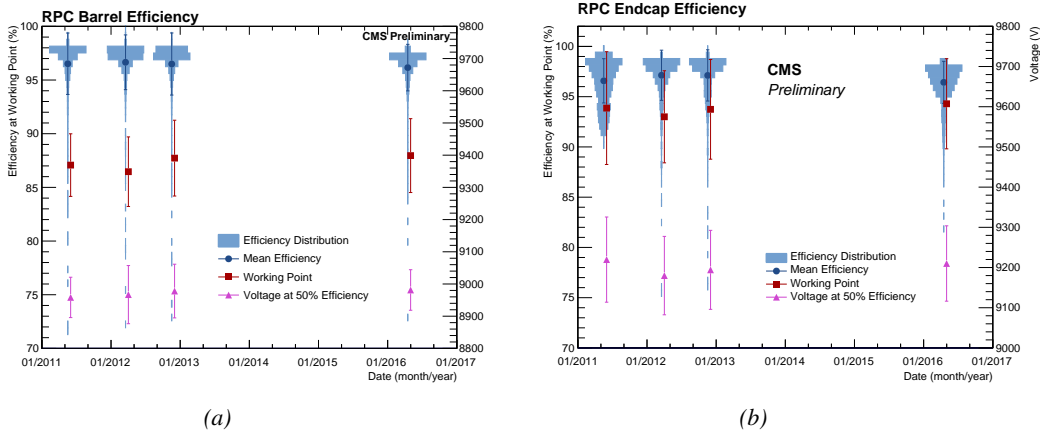


Figure 4.25: Evolution of the efficiency, working voltage, and voltage at 50% of maximum efficiency for CMS Barrel (a) and Endcap (b) RPCs obtained through yearly voltage scans since 2011. The working voltage of each RPC is updated after each voltage scan to ensure optimal operation [261].

3306 It was already discussed that in the future, it is likely that the use of freon gases could be banned.
 3307 Using CF_4 , $C_2H_2F_4$ and SF_6 , both CSC and RPC subsystems will need to address this problem
 3308 by finding new gas mixture for the operation of their detectors. Finding a replacement for these gas
 3309 components that were used for very specific reasons is a great challenge. Indeed, CSCs use CF_4 in
 3310 order to enhance the longevity of the detectors, increase the drift velocity of electrons and quench
 3311 photons with a non-flammable gas mixture. RPCs use a mixture mainly composed of $C_2H_2F_4$, or
 3312 $R134a$, that features a high effective Townsend coefficient and the great average fast charge allowing
 3313 for operations with a high threshold. The mixture also contains a small fraction of SF_6 that is used
 3314 for its electronegative properties that prevents the development of delta-rays in the gas volume that
 3315 might trigger multiple ionization and avalanches. It only represents 0.3% of CMS standard mixture
 3316 but more than 5% of its overall GWP.

	CSC	RPC
Greenhouse gases used	CF_4	$C_2H_2F_4$ and SF_6
Greenhouse gases fraction in the gas mixture	10%	95.2% and 0.3%
Global Warming Potential (relative to CO_2)	6500	1300 and 23900
Gas mixture re-circulation	Yes, 90%	Yes, 85%
Gas mixture replenishing rate (l/hr)	700	1100
F-gas recuperation	Yes, $\approx 40\%$	No
F-gas venting rate (l/hr)	42	1047 and 3.3
CO_2 -equivalent rate (m^3/h)	273	1440
Relative impact (entire muon system = 100%)	16%	84%

Table 4.1: Details of the greenhouse fluorinated gases used in CMS and of their GWP [177].

3317 All these gases have a very high GWP, as reported in Table 4.1, and only few options are left. The
 3318 subsystems need to work on strongly decreasing the loss of these gases due to leaks in the gas system

3319 or need to completely change their gas mixture for more ecofriendly ones. Reducing the amount of
 3320 F-gas released in the atmosphere due to leaks on the current gas system will require installation of
 3321 a F-gas recuperation system on RPCs side and an upgrade of CSCs existing one in addition to the
 3322 repair of existing leaks. With such measures, it is expected that the total rate of greenhouses gas
 3323 vented in the atmosphere would represent only 1.6% of the current levels [177]. In the most critical
 3324 case the F-gas were to be banned, it would be necessary to have replacement mixtures to operate
 3325 CMS. CSC is presently investigating replacement for CF_4 such as CF_3I , C_4F_6 , IC_3F_6 , C_3F_8 or
 3326 CHF_3 . RPCs, in collaboration with the ATLAS RPC group which uses the same gas mixture, have
 3327 identified CF_3I ($GWP \leq 1$) and $C_3H_2F_4$ ($GWP \sim 6$), referred to as *HFO-1234ze*, as potential
 3328 candidates with mixtures containing CO_2 . CO_2 is already widely used by various RPC experiments
 3329 in mixtures with argon. More R&D needs to be conducted for both subsystems before concluding
 3330 on the best alternative. Finding no good alternative to the present mixtures will require very efficient
 3331 abatement system in CMS to burn and convert the greenhouse gases into less harmful ones. This
 3332 way, the air pollution would be strongly reduced.

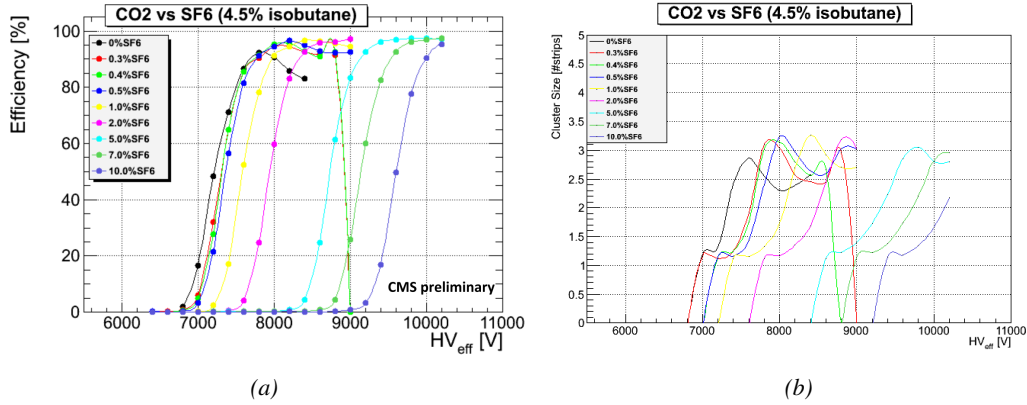


Figure 4.26: Efficiency (a) [203] and cluster size (b) of a standard double-gap RPC operated with CO_2 mixtures for different ratios of SF_6 .

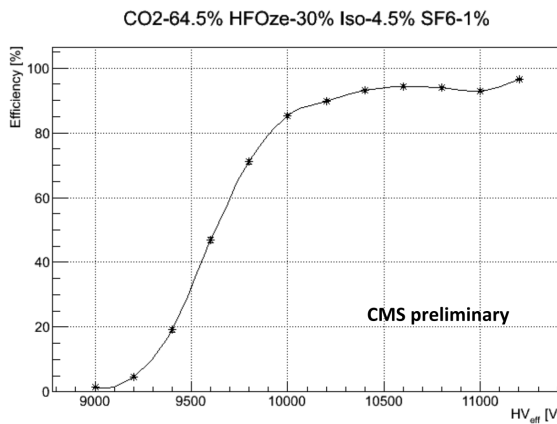


Figure 4.27: Efficiency of a CMS double-gap RPC operated with 30% of HFO , 4.5% of iC_4H_{10} , 1% of SF_6 and 64.5% of CO_2 [203].

Preliminary studies conducted in Ghent confirmed that CO_2 alone would require more than 1% of SF_6 to reach full efficiency, as presented in Figure 4.26. Even though the results obtained in Ghent don't show the streamer probability (the probability to have very large avalanches whose induced charge is greater than 20 pC), the variation of the cluster size indicates that the streamers become predominant before the efficiency plateau is reached. Then, a very first test with an HFO/CO_2 was performed. Only one ratio was tested as can be seen from Figure 4.27 that displays a good efficiency with a plateau located at a similar high voltage than with $R134a$ based mixtures (Figure 4.28). The status of RPC studies is presented in Figure 4.28 in which the performance (efficiency and streamer probability) of a CMS double-gap RPC operated with alternative gas mixtures is compared to the present CMS RPC mixture. Although the efficiency of detectors operated with mixtures containing CO_2/CF_3I or CO_2/HFO as a replacement for $C_2H_2F_4$ seems to reach similar levels than which of the detectors operated with the present mixture, the new gas mixtures feature a streamer probability that far exceeds which of the present fluorinated mixture. The SF_6 doesn't seem to prevent the formation of streamers as efficiently even when used at levels more than three times higher than with the standard CMS RPC mixture. Nevertheless, it is important to note that these results were obtained with a single-gap RPC while the use of a double-gap RPC reduces the operation voltage by 200 to 300 V, lowering the induced charge. A compromise in between good efficiency and acceptable level of streamer probability, and the fine-tuned composition of potential replacement gas mixtures will be kept on being studied using a standard double-gap CMS RPC.

Although the technology certification was conducted with the standard CMS gas mixture which is a known reference, the iRPCs will need to be operated with new environmental-friendly gas mixtures. Studies have then been conducted with iRPCs, assuming that the HFO/CO_2 mixture contain-

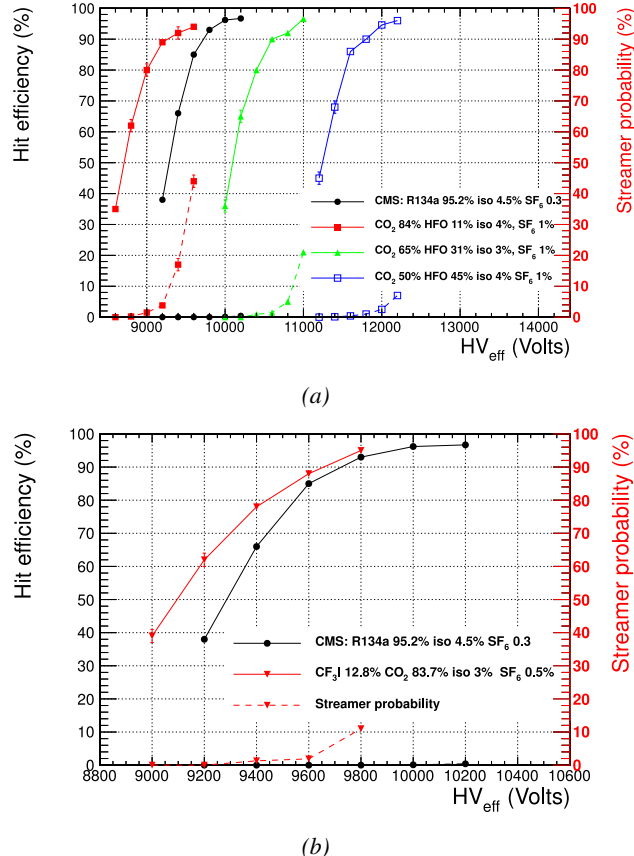


Figure 4.28: The efficiency (solid lines) and streamer probability (dashed lines) of HFO/CO_2 (a) and CF_3I/CO_2 (b) based gas mixtures as a function of the effective high-voltage are compared with the present CMS RPC gas mixture represented in black [177, 203]. The detector used for the study is a single-gap RPC with similar properties than CMS RPCs. The streamer probability is defined as the proportion of events with a deposited charge greater than 20 pC.

ing an almost equal level of both components was the most likely candidate to replace the standard mixture. In this purpose, an iRPC prototype has been built to be tested with an HFO/CO_2 gas mixture. The mixture, referred to as "ecogas" in Figure 4.29, contained 50% of HFO , 4.5% of iC_4H_{10} , 0.3% of SF_6 and 45.2% of CO_2 . In Figure 4.29 is presented a result consistent with the blue curve obtained with 45% of HFO , 4% of iC_4H_{10} , 1% of SF_6 and 50% of CO_2 flushed into a standard double-gap RPC. Instead of the streamer probability, the cluster size is shown. The average number of hits generated by a muon passing through the chamber seem to have increased by 1 at the level of the knee of the sigmoid plateau using the ecogas.

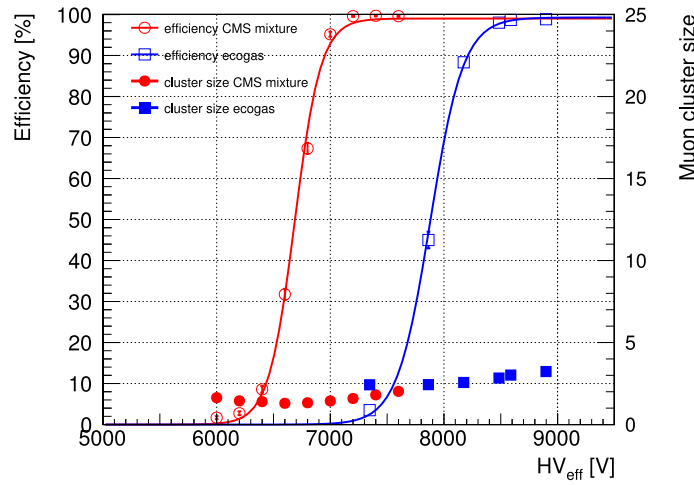


Figure 4.29: Efficiency (open symbols) and cluster size (full symbols) of an iRPC as a function of the effective voltage for the standard CMS gas mixture and an environmental-friendly gas mixture [177].